

Chair of Optoelectronics  
Institute for Computer Engineering  
Ruprecht-Karls-University Heidelberg

# Annual Report 2012

# CONTENTS

Staff .....	II
Foreword .....	III
Research Projects .....	IV
Publications in 2012 .....	12
Imprint.....	13

# STAFF



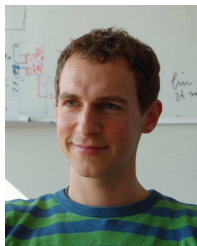
**Prof. Dr. Karl-Heinz Brenner**  
Lehrstuhlinhaber



**Fernando Merchán Alba**  
Wissenschaftlicher Mitarbeiter



**Dr. Xiyuan Liu**  
Wissenschaftliche Mitarbeiterin



**Maximilian Auer**  
Wissenschaftlicher Mitarbeiter



**Wolfgang Stumpfs**  
Technischer Angestellter



**Eike Slogsnat**  
Wissenschaftlicher Mitarbeiter



**Tim Stenau**  
Wissenschaftlicher Mitarbeiter



**Sabine Volk**  
Sekretariat



**André Junker**  
Student



## FOREWORD

Dear reader,

This annual report describes the research activities of the chair of optoelectronics for the year 2012. Since the activities on optical interconnects have moved to a ziti-research group, only one contribution is dealing with this topic now. Also the Viroquant project has finally run out. Several new activities are concentrating around a new phase element - the overlapping micro lens array which has several nice theoretical aspects and also a number of interesting applications, including high NA focusing and phase retrieval. Another central part of research concerns computational optics, where new findings are reported. In one contribution, we found that the various near field calculation methods are not equivalent when it comes to local absorption. In another contribution we explain why oblique illumination should not be modeled by a linear phase factor. One contribution picks up on an old problem, the inclination factor for high NA focusing, where we found that realistic focusing optics differs significantly from the theoretical model.

We hope that many of the topics in this report will find your interest.

Karl-Heinz Brenner  
*Head of the chair*

# RESEARCH PROJECTS

<b>Integration of micro-optical and electronic systems for the fabrication of Active Optical Cables</b> <i>F. Merchán, K.-H. Brenner</i> .....	1
<b>Impact of different field calculation methods on local light absorption in periodic structured media</b> <i>M. Auer, K.-H. Brenner</i> .....	2
<b>Optimization of local absorption in layered media</b> <i>K.-H. Brenner</i> .....	3
<b>Talbot Focusing – A new effect of periodic structures and its utilization</b> <i>R. Buschlinger, K.-H. Brenner</i> .....	4
<b>Design of a diffractive micro lens array for Shack-Hartmann wavefront sensing</b> <i>T. Stenau, K.-H. Brenner</i> .....	5
<b>Diffractive micro lens arrays with overlapping apertures – design, fabrication and application</b> <i>X. Liu, T. Stenau, K.-H. Brenner</i> .....	6
<b>Sensitivity-enhanced complex amplitude retrieval using multi-plane intensity detection and a micro lens array</b> <i>X. Liu, K.-H. Brenner</i> .....	7
<b>Accelerated calculation of z-scans in numerical light propagation</b> <i>K.-H. Brenner</i> .....	8
<b>On the true inclination factor under realistic focusing conditions</b> <i>K.-H. Brenner</i> .....	9
<b>Treatment of oblique illumination in numerical light propagation</b> <i>K.-H. Brenner</i> .....	10
<b>Imaging properties of a multi-spectral fluorescence microscope</b> <i>E. Slognat, P. Fischer, K.-H. Brenner</i> .....	11

# Integration of micro-optical and electronic systems for the fabrication of Active Optical Cables

F. Merchán, K.-H. Brenner

In recent years, the development of active optical cables has been incentivized by the requirements of the rapidly growing high performance computers and correspondingly the interconnections market, moreover, the optimization of the fabrication process and the development of smart and efficient solutions has become a research topic.

The most important factors that must be considered already in the design phase are the feasibility with available technology, costs and the possibility of automation of the fabrication and adjustment processes. The fabrication of AOC's is driven by these factors; consequently, all processes involved have to be optimized in order to meet the requirements.

The replication of metal masters for the fabrication of optical couplers has been confirmed as a very accurate and cost effective method. In order to complete the optimized fabrication chain, the optical systems have to be integrated with the electronics, which is fabricated with well-known, available methods. For this purpose, a modular construction is implemented so that the optical- and the electronic sub-systems are constructed and after their functionality is proven, the systems are aligned using standard mechanics. The constructed system has 5 degrees of freedom: the cartesian coordinates and two tilt angles that are critical to achieve the desired coupling efficiency. The tilt angle around the transversal axis of the VCSEL array is the most critical one (see Fig. 1). Measurements show that this angle is up to  $2.3^\circ$  in the worst case for a standard manual flip-chip process. This precision is inherent to the used laboratory machine and might be better in current automated industrial processes.

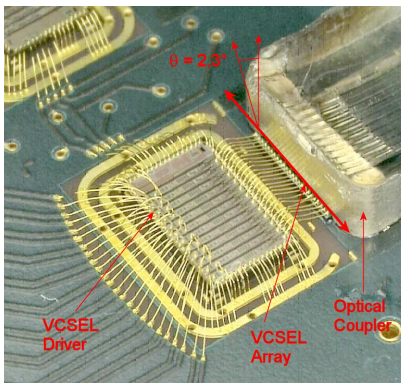


Fig. 1 Adjustment of the coupler on the PCB

With this angle adjusted, a coupling efficiency of about 50% can be assured. For systems that are some meters in length (up to 10m), this coupling efficiency is acceptable. In order to reach higher coupling efficiencies, an active adjustment is required. The Fig. 2, shows the coupling efficiencies that can be reached with passive alignment and the improvement if active alignment is made. When using active alignment the coupling efficiency is, in the worst case, about 90%; which

represents a considerably higher efficiency than that reached using passive alignment.

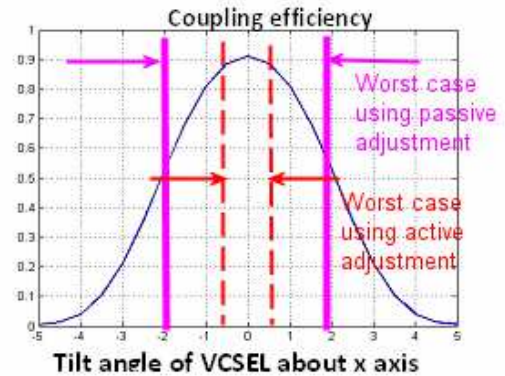


Fig. 2: Coupling efficiency on tilt angle dependency

Optical couplers, VCSEL-Driver, VCSEL-Array, Transimpedance-Amplifier and Photodiode-Array are integrated in a  $22 \times 25 \text{ mm}^2$  and 3mm height PCB (see Fig.3). With commercially available devices it is possible to achieve up to 12.5 Gbit/s per channel and in the complete AOC up to 300 Gbit/s duplex.

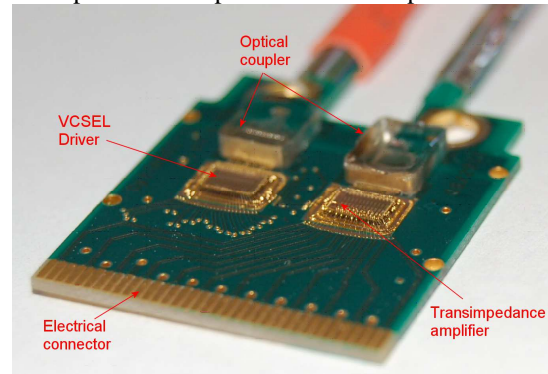


Fig. 3: Fabricated Active Optical Cable

## References:

- [1] F. Merchán, K.-H. Brenner, „Novel integrated micro-optics system for the fabrication of Active Optical Cables“, (Online-Zeitschrift der Deutschen Gesellschaft für angewandte Optik e. V.), ISSN: 1614-8436-urn:nbn:de:0287-2012-B036-5, 113. Jahrestagung, 29. Mai-02. Juni 2012, Eindhoven, (2012)
- [2] K.-H. Brenner, „Aspekte der Lichtausbreitung zwischen verkippten Ebenen“, Jahrestagung der Deutschen Gesellschaft für angewandte Optik e. V. in Wetzlar (2010)

# Impact of different field calculation methods on local light absorption in periodic structured media

M. Auer, K.-H. Brenner

Precise knowledge of the spatial location of light absorption in structured media is needed for the optimization of optoelectronic devices like detectors, solar cells or photolithographic systems. Recently we reported a definition for local absorption, which is derived from electromagnetic near fields [1]:

$$a(\mathbf{r}) = \frac{k_0^2}{k_{\text{inc},z}} \frac{1}{A} \text{Im}(\epsilon(\mathbf{r})) \cdot |\mathbf{E}_1(\mathbf{r})|^2 \quad (1)$$

Unlike the global absorption  $A$ , where energy conservation is obtained by definition,

$$A = 1 - \text{Transmission} - \text{Reflection} \quad (2)$$

the local absorption  $a$  depends on the method of field calculation, which is not unique.

In the RCWA algorithm the inverse Li-rule [2] improves stability in the calculation of reflection and transmission coefficients in case of complementary discontinuities in permittivity and field. The standard field calculation approach uses the same inverse rule, expressed by the mode limited Matrix  $\mathbf{E}_a^{-1}$ :

$$E_x = \sum_m e_m(z) e^{ik_{x,m}x}, \mathbf{e}(z) = -i \mathbf{E}_a^{-1} (\mathbf{W} \cdot \mathbf{Q} \cdot \mathbf{D}(z)) \quad (3)$$

Due to the discontinuity of the materials at boundary surfaces, a second method, introduced by Lalanne and Jurek (PLMJ) [3], derives the E-field from a continuous D-field and multiplies with the original non-mode limited permittivity  $\epsilon(x)$ :

$$E_x = \frac{1}{\epsilon} \sum_m d_m(z) e^{ik_{x,m}x}, \mathbf{d}(z) = -i (\mathbf{W} \cdot \mathbf{Q} \cdot \mathbf{D}(z)) \quad (4)$$

In a third method (KHB) Brenner [1] likewise derives the E-field from a continuous D-field. But because the material distribution is mode-limited and thereby continuous, he returns to a purely mode-limited implementation, avoiding the inverse Li-rule:

$$E_x = \sum_m e_m(z) e^{ik_{x,m}x}, \mathbf{e}(z) = -i \mathbf{E}^{-1} (\mathbf{W} \cdot \mathbf{Q} \cdot \mathbf{D}(z)) \quad (5)$$

In order to compare the various field calculation methods in two- and three-dimensional structured media, we introduced three criteria:

Our first criterion is based on convergence. We compare low mode count results to a converged, high mode count result. Secondly we check Maxwell's continuity conditions, which require tangential field components to be continuous. The third criterion tests conservation of energy, which in this case means an agreement of global absorption (eq. 2) and integrated local absorption (eq. 3) over the full grating:

$$A = \iiint a(\mathbf{r}) dV \quad (6)$$

In a test case, a 2D absorbing GaAs-grating is illuminated with a TM-polarized plane wave ( $\lambda = 1\mu\text{m}$ ). The global absorption from RCWA is 1.39%.

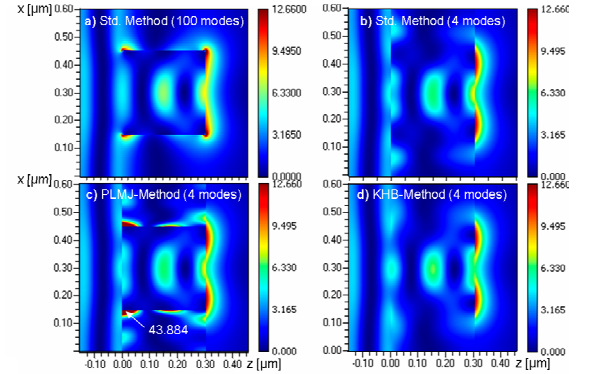


**Fig. 1:** Different field calculation methods and their effect on local absorption. Integrated absorption (and deviation):  
a) Std. method (100 modes): 1.447% (= +4.1% dev.)  
b) Std. method (4 modes): 1.475% (= +6.12% dev.)  
c) PLMJ-method (4 modes): 1.391% (= +0.14% dev.)  
d) KHB-method (4 modes): 1.398% (= +0.58% dev.)

In the two-dimensional case (fig 1) we can see that for a small mode count the PLMJ-method and the KHB-method both satisfy the third criterion much better than the standard method. While the PLMJ-method has more visual similarities with the converged field solution, the KHB-method brings in self-consistency by staying compatible with the mode limitation of the RCWA. In the three-dimensional case the results are less clear. Here the results strongly depend on system geometries (fig 2). Nevertheless the three criteria are a useful instrument to validate simulation results with small mode counts.

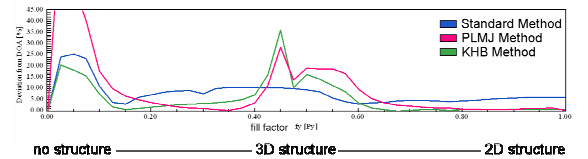


**Fig. 2:** Deviation between global absorption and integrated local absorption for various three-dimensional grating

## References:

- [1] K.-H. Brenner, „Aspects for calculating local absorption with the rigorous coupled-wave method“, Opt. Express, 10369-10376, 2010
- [2] L. Li. New formulation of the Fourier modal method for crossed surface-relief gratings. Opt. Soc. Am. A 14(10): 2758–2767, 1997
- [3] P. Lalanne and M.P. Jurek, „Computation of the near-field pattern with the coupled-wave method for transverse magnetic polarization“, Journal of Modern Optics, Vol. 45, No. 7, 1357-1374, 1998



# Optimization of local absorption in layered media

*K.-H. Brenner*

Local absorption plays an important role in all semiconductor detectors and solar cells. Since all the standard multilayer stack theories only provide global absorption, being defined as the difference of incoming power and the sum of reflected and transmitted power, information is lost, concerning the exact position along the stack, where absorption takes place. In semiconductors, the photon to electron conversion is most efficient, if the absorption takes place at or near the depletion layer, while absorption at other positions only contributes to heat generation. Being able to compute local absorption, allows an optimization of a structure with respect to conversion efficiency.

The theoretical basis for describing local absorption has been published in [1] for the standard RCWA-implementation. For a stack of layers with different thicknesses and permittivities, a different approach using Poynting vector differences was recently published in [2]. Our theory of local absorption can be adapted to a layer stack [3] in a straight forward manner and shows perfect numerical agreement with the results in [2].

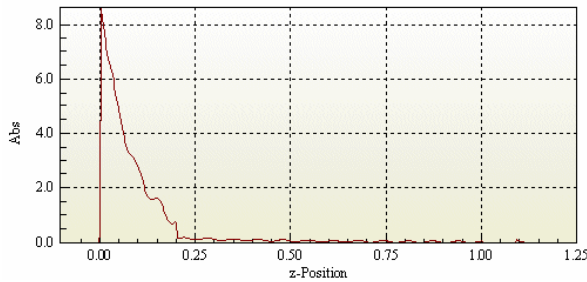


**Fig. 1:** Local absorption  $a(z)$  for a typical solar cell structure. Most of the light is absorbed at the interface between air and the amorphous silicon layer.

If the layers are assumed constant in the x-y plane and z is the direction along the stack, we define the integrated absorption by

$$A_{z_1, z_2} = \int_{z_1}^{z_2} a(z') dz' \quad (1)$$

It describes the ratio of incident power to the power absorbed in the interval between  $z_1$  and  $z_2$ . Using the equations derived in [1], we can write the local absorption quantitatively as

$$a(z) = \frac{\partial A(z)}{\partial z} = \frac{k_0^2}{k_{z,i}} \text{Im}(\epsilon) |\mathbf{E}_1(z)|^2 \quad (2)$$

Here,  $k_{z,i}$  is the z-component of the incident k-vector,  $\epsilon$  is the permittivity of the medium at position z and

$\mathbf{E}_1$  is the local electric field, resulting from an incident electromagnetic plane wave with an electric field amplitude of one. Note that  $a(z)$  has a dimension of 1/m and  $A_{z_1, z_2}$  is dimensionless since it describes a ratio.

For a layered stack of amorphous silicon, polysilicon, silicon oxide and steel, as is usual in solar cells, we can calculate the local absorption for different layer thicknesses. A typical profile is shown in fig. 1. As one can see, most of the light is absorbed at the interface between air and the amorphous silicon layer, while very little light is absorbed near the a-Si - poly-Si interface.

By varying the thickness of the first two layers, a map (fig. 2) for the absorption in a given region can be computed, which may serve as the basis for optimizing absorption in the desired region.

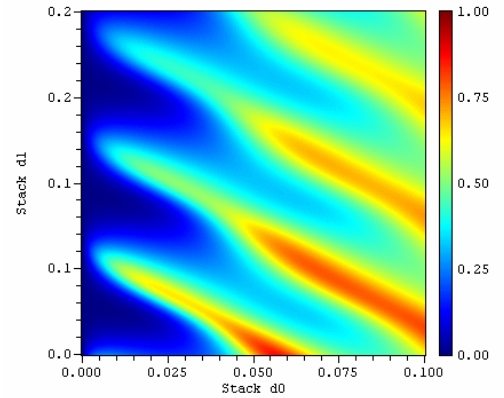


**Fig. 2:** Variation of the thicknesses of layer 1 and layer 2 shows pronounced absorption maxima in layer 0, which can be used for optimization

The optimization of a detector structure is of equal importance, since the increase in photo current goes along with a reduction in heat generation. The technique can also be extended to polychromatic light.

## References:

- [1] Karl-Heinz Brenner, „Aspects for calculating local absorption with the rigorous couple-waved method“, *Opt. Express*, 18, 10369-10376, (2010).
- [2] O. Deparis, "Poynting vector in transfer-matrix formalism for the calculation of light absorption profile in stratified isotropic optical media", *Opt. Lett.* 36, 3960-3962 (2011).
- [3] K.-H. Brenner, "Optimization of local absorption in layered media", 8th EOS Topical Meeting on Diffractive Optics, Delft/NL, (2012)



# Talbot Focusing - A new effect of periodic structures and its utilization

R. Buschlinger, K.-H. Brenner

The Talbot effect is a well known phenomenon of self imaging, stating that either an amplitude or a phase distribution is replicated at the Talbot distance. Talbot imaging can also be observed at fractional Talbot distances [1] for special distributions. Talbot Focusing is a new effect, by which a highly concentrated focal spot appears at a particular distance from the periodic optical element. With this effect, the spot diameter is independent of the structure period and the focal length, enabling high NA-foci with large working distance or which are placed very dense.

By observing the intensity pattern behind a simple amplitude Ronchi grating (see fig. 1), we see various effects. At the Talbot distance (here at 200 units), a perfect image of the input distribution is visible. At half the distance, a contrast inverted pattern is observed. What is most important, is that there are also certain distances, where pronounced on-axis focal spots appear.

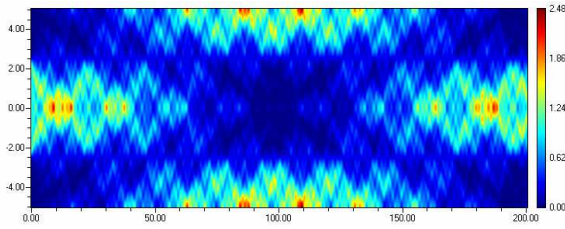


**Fig. 1:** Light distribution  $I(x,z)$  behind a simple amplitude Ronchi grating. In addition to Talbot images, there are also focal spots on the optical axis.

These focal spots can be much smaller than focal spots generated with a micro lens of the same diameter. If we zoom into the first region between 0 and 50 units, we see, that these foci are not only very concentrated in the lateral direction but also in the longitudinal direction.

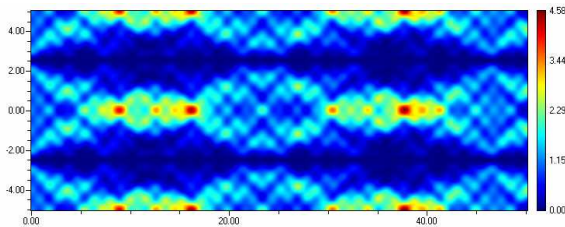


**Fig. 2:** Zoom into the intensity distribution of fig. 1

A necessary condition for a focal spot is that the on-axis amplitude has a maximum. Taking into consideration, that the complex input transmittance is

periodic, we can apply angular spectrum propagation for a periodic field and obtain

$$u_z(0,0) = \sum_{n,m} U_{m,n} e^{4\pi i \frac{\zeta}{\Lambda^2} \sqrt{1-\Lambda^2(m^2+n^2)}} \quad (1)$$

where  $\zeta = \frac{z}{z_T}$  is the z-position relative to the Talbot

length and  $\Lambda = \frac{\lambda}{P}$  is the optical wavelength in units of the element period.  $U_{m,n}$  are the Fourier coefficients of the input transmittance. From eq. 1 it is clear, that  $u_z(0,0)$  is maximized, when

$$U_{m,n} = e^{-4\pi i \frac{\zeta}{\Lambda^2} \sqrt{1-\Lambda^2(m^2+n^2)}} \quad (2)$$

A similar result has been obtained independently in [4]. With this result, quite unusual focusing arrays can be designed. In one extreme, an array with a numerical aperture of one was obtained for 1 mm focal distance and 32  $\mu\text{m}$  period. In another extreme, an array with a pitch of 300  $\mu\text{m}$  and a focal length of 10 cm was obtained.

These elements may find a large number of applications. The extremely long focal length elements e.g. can be used for the detection of wave-front tilts with an accuracy of  $10^{-6}$ . The high NA-elements can be used for scanning a microscopic sample with a high degree of parallelism.

## References:

- [1] A. W. Lohmann, "An array illuminator based on the Talbot effect", *Optik*, 79, 41 – 45 (1988)
- [2] R. Buschlinger, K.-H. Brenner, „Light Focusing by binary phase gratings“, 5th EOS Topical Meeting on Advanced Imaging Techniques (AIT), Engelberg/Ch (2010)
- [3] K.-H. Brenner, R. Buschlinger, „Parallel image scanning with binary phase gratings“, *Journal of European Optical Society : Rapid Publications* 6, 11024 (JEOS:RP), (2011)
- [4] S. Stallinga, "High-NA diffractive array illuminators", EOS Topical meeting on Diffractive Optics, 2012 Delft, No. 4932.

# Design of a diffractive micro lens array for Shack-Hartmann wavefront sensing

T. Stenau, K.-H. Brenner

A common method to measure the aberrations of a wave front is the use of a Shack-Hartmann wavefront sensor. The two main components of this sensor are a refractive micro lens array with a given period and focal length, and a camera sensor which is placed in the focal plane of the micro lens array.

An ideal wavefront produces a regular spot pattern on the camera. The spot pitch ( $P$ ) is determined by the pitch of the micro lens array. For a wavefront with small aberrations, the spots are shifted according to the local tilt of the incoming wave. From the spot shift, the gradient of the wavefront can be determined. The accuracy of the wavefront measurement depends on the accuracy of the measured spot shifts, which again depends on the sensor pixel size.

The spot shift is linear proportional to the focal length, thus the accuracy can be increased with longer focal lengths. Using refractive micro lenses, however, there is a limit with respect to the focal length ( $f$ ), since the diameter of the focal spot increases with decreasing numerical aperture ( $NA$ ). When the spot size exceeds the pitch, the accuracy limit is reached.

By using a diffractive micro lens array, we are able to avoid this problem. For these lenses,  $NA$ ,  $f$  and  $P$  can be chosen independently [1]. This is possible, since diffractive micro lenses can be designed with overlapping aperture. Therefore, a long focal length can be combined with small focal spots, allowing a detection of very small wavefront tilts.

We designed and produced a binary diffractive micro lens array consisting of  $22 \times 28$  replicas of a  $320 \mu\text{m} \times 320 \mu\text{m}$  elemental cell. The primitive cell has a resolution of  $128 \times 128$  pixels and is shown in figure 1. For the focal length we chose 10 cm at the HeNe laser wavelength of 633 nm and the design  $NA$  was chosen to 0.02.

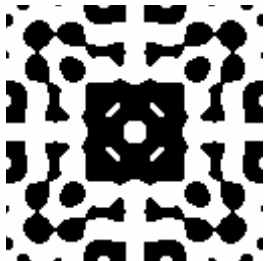


Fig. 1: Primitive cell of the diffractive micro lens array.

In a lithographic process we transferred this structure to a float glass substrate coated with photoresist. The height of the developed photoresist resulted in a phase shift of  $\pi$ . A microscope image of the produced diffractive micro lens array is shown in figure 2.

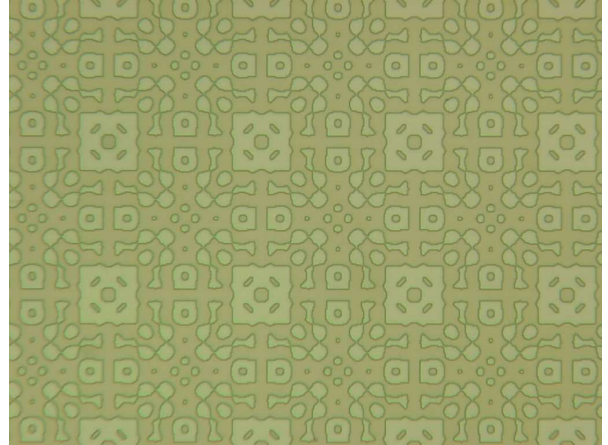


Fig. 2: Microscope image of a few primitive cells of the produced diffractive micro lens array.

In a numerical simulation, we illuminated the element with a plane wave. The cross section of the amplitude in the designed focal plane at  $z = 10$  cm is shown in figure 3.

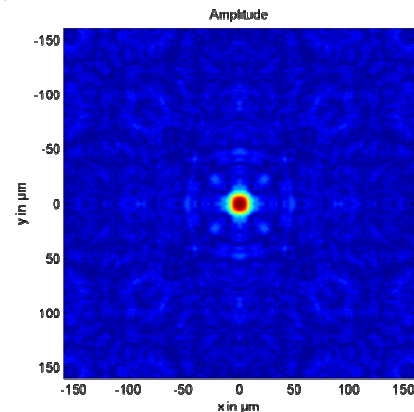


Fig. 3: Amplitude in the designed focal plane.

The spot size of a comparable refractive micro lens array with the same focal length and pitch would be  $400 \mu\text{m}$ , which is significantly larger than the pitch. Here, the width of the focal spot is approx.  $20 \mu\text{m}$ . For a CCD with  $2 \mu\text{m}$  pixel size, a spot shift of  $0.5 \mu\text{m}$  is safely detectable. Thus, the achievable angular resolution should be better than  $5 \cdot 10^{-6}$ . The performance of this new type of Shack-Hartmann sensor is presently investigated by a group at the Laser-Laboratorium Göttingen e.V.

## References:

- [1] X. Liu, T. Stenau K.-H. Brenner, „Diffractive micro lens arrays with overlapping apertures”, 11<sup>th</sup> Euro-American Workshop on Information Optics (WIO 2012)

# Diffractive micro lens arrays with overlapping apertures – design, fabrication and application

X. Liu, T. Stenau and K.-H. Brenner

Diffractive micro lens arrays offer a fundamental advantage over refractive ones: the effective numeric aperture (NA) can be selected independent of the lens pitch and the focal length. The cell NA is defined by

$$NA_{cell} = \frac{P}{\sqrt{P^2 + 4f^2}} \quad (1)$$

where  $P$  is the pitch and  $f$  the focal length of the micro lens array. The effective NA is given by the diameter of the pupil (magenta in fig. 1). If the effective NA is larger than the cell NA, an overlapping micro lens array is realized. By lens overlapping, a dense array with large working distance and high numerical aperture is possible.

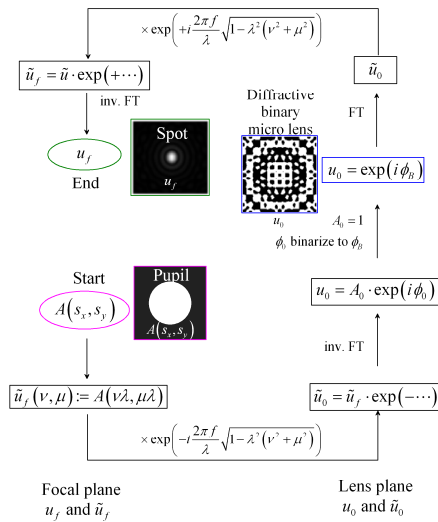


**Fig. 1:** Design procedure: pupil function (magenta); diffractive binary micro lens (blue); spot diagram (green).

The design procedure, shown in figure 1 is similar to the method in reference [1]. With this design procedure, the effective NA, the focal length and the pitch of each micro lens can be chosen independently. In figure 2 we compared a refractive micro lens array with a diffractive one, where both had a lens pitch of  $256\mu\text{m}$  and a focal length of  $10\text{mm}$ . The NA of the refractive micro lens is  $0.0128$ , equal to the cell NA. The effective NA of the diffractive micro lens is  $0.036$ , about 2.8 times larger than the cell NA. Due to the overlapping aperture, the diffractive focal spot is clearly sharper than the refractive one.

For the fabrication of diffractive micro lens arrays, we applied our laser lithography. The photo resist was Shipley S1805. Here for simplicity, we used the resist layer as the phase structure and the measured phase shift deviated from  $\pi$  only by a few percent. In figure 3 we show a microscope image of the fabricated micro lens and the focal intensity by illumination with a laser

diode. The line plots through one focal spot confirm a good agreement between calculated and measured spot intensities.

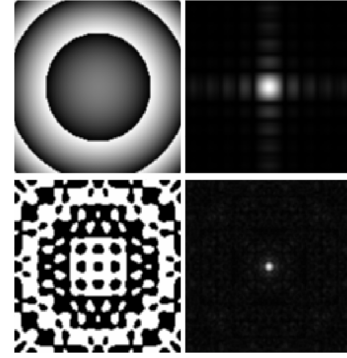


**Fig. 2:** Comparison of a refractive micro lens (top) and a diffractive one with overlapping aperture (bottom). In both cases,  $f = 10\text{ mm}$ ; phase (left) and focal amplitude (right).

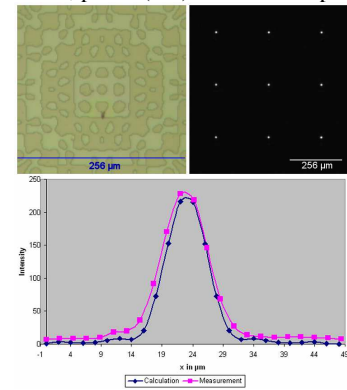


**Fig. 3:** Microscope picture of fabricated micro lens (top left), intensity spot diagram with  $3 \times 3$  focal spots shown (top right), line scans of calculated and measured spot intensity (bottom)

In one of our current projects, such an overlapping diffractive micro lens array was applied to multi-plane iterative phase retrieval. By applying a diffractive micro lens array to Hartmann-Shack wave front sensing, the spot density can be increased without changing the focal length, thus enabling a higher spatial resolution. Further applications are multi-spot scanning microscopy or light concentration [1, 2].

## References:

- [1] D. Hulsken, S. Vossen and S. Stallinga: "High-NA diffractive array illuminators and application in a multi-spot scanning microscope", J. Europ. Opt. Soc. Rap. Public. 12026 Vol. 7 (2012)
- [2] K.-H. Brenner and R. Buschlinger: "Talbot Focusing – a new effect of periodic structures and its utilization", DGaO Annual meeting in Eindhoven, Netherlands (2012)

# Sensitivity-enhanced complex amplitude retrieval using multi-plane intensity detection and a micro lens array

X. Liu and K.-H. Brenner

Phase retrieval methods like the classical Gerchberg-Saxton algorithm have an advantage compared to interferometric and holographic methods, in that they require no reference wave. Thus no laser is required and the set-up can be very simple and stable. Pedrini has extended this method to obtain the complex amplitude from a sequence of diffraction intensities [1, 2]. Unfortunately, the method is only reliable for non-smooth phase distributions. For smooth phase distributions, the intensity change along the propagation direction  $z$  is too small for a reliable reconstruction, thus phase retrieval is only possible with highly increased  $z$ -sampling. Here we propose an extension of his method by including a micro lens array, similar to a Hartmann-Shack-sensor (HS). The lens enhances the intensity variation of the recorded intensity patterns and it is numerically easy to eliminate from the recovered phase distribution. The improved performance of the algorithm is firstly demonstrated by numerical simulations.

For HS-sensing, only the focal plane intensity is used to recover the wave front and the spatial sampling of the wave front is determined by the micro lens pitch. Classical HS-sensing is reliable only for smooth phases and the resolution is limited by the pitch. By combining the HS-sensor with multi-plane phase retrieval, the limitations of both methods can be removed. Here, a sequence of intensity measurements performed symmetrically around the focal plane is recorded and used to recover the wave front (figure 1). With this method, a phase distribution with both, smooth and non-smooth contributions can be reliably reconstructed.

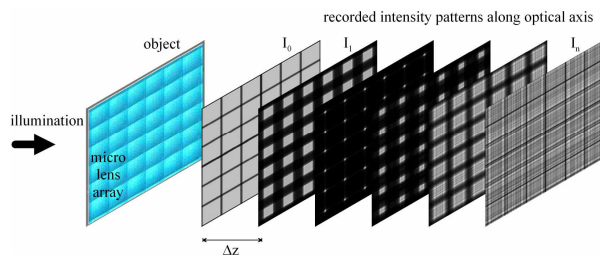


**Fig. 1:** Scheme for multi-plane measurement of intensity around the focal plane

Figure 2 shows a simulation result for recovering an inclined plane wave (left). Without the introduction of the auxiliary micro lens array, the intensity patterns at every propagation distance would be identical, resulting in a global constant as the reconstructed phase, which is obviously incorrect. With a refractive  $8 \times 8$  lens array placed at  $z = 0$ , the intensity patterns show a variation, i.e. focusing and spot shift, which

makes the recovery of complex amplitude possible. However, within each micro lens window there is one unknown constant phase shift (middle), which was removed by additional unwrapping and stitching (right).

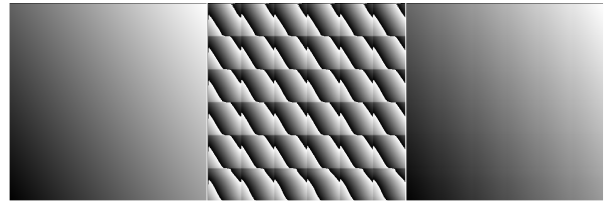


**Fig. 2:** Simulation result for the recovery of an inclined plane wave from 20 intensities and 2 iterations. Left: initial phase distribution; middle: recovered wrapped phase distribution, greyscale corresponds to phase: white =  $\pi$ , black =  $-\pi$ ; right: recovered phase after unwrapping and stitching.

Figure 3 shows a simulation result for recovering the sum (left background) of a smooth (left top) and a non-smooth (left bottom) phase. Using the standard method, the smooth part of the phase will be lost. With this method, the reconstruction (right) is valid, confirming that the proposed method is reliable for both smooth and non-smooth phase distributions.

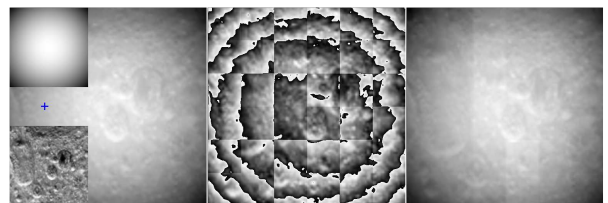


**Fig. 3:** Simulation result to confirm that the proposed method is reliable for both smooth and non-smooth phase distributions (explanation: see text). The reconstruction was done with 20 intensity patterns and 2 iterations. Middle: recovered wrapped phase distribution; right: recovered phase after unwrapping and stitching.

## References:

- [1] G. Pedrini, W. Osten and Y. Zhang: "Wave-front reconstruction from a sequence of interferograms recorded at different planes", *Opt. Lett.*, Vol. 30, 833-835 (2005)
- [2] P. Almoró, G. Pedrini and W. Osten: "Complete wavefront reconstruction using sequential intensity measurements of a volume speckle field", *Appl. Opt.*, Vol. 45, 8596-8605 (2006)



# Accelerated calculation of z-scans in numerical light propagation

*K.-H. Brenner*

The numerical treatment of light propagation usually occurs between two planes perpendicular to the optical axis. In this case, an x-y-section (see fig. 1, blue) is calculated and displayed.

For the analysis of focused beams, for wave guides, for Talbot carpets or in imaging situations for the investigation of depth of focus, also a x-z-section or a y-z-section (see fig. 1, green) is of interest. Fig. 2 shows such an example, where the focus for a thin element lens with a parabolic phase profile and a numerical aperture of 0.15 was analysed. The figure displays the amplitude instead of the intensity in order to enhance the low amplitude components.

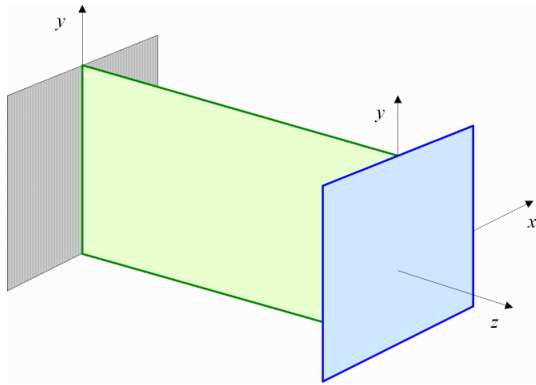


**Fig. 1:** Illustration of a x-y-section (blue) and a y-z-section (green)

The brute force method for obtaining such a z-scan is to select a start position  $z_0$  and a z-step  $dz$  and then to perform  $NZ$  single propagation operations, where in each propagation step, a horizontal or vertical line is extracted from the 2D-data. The combination of these lines to an image results in the desired z-scan.

The time for this brute force approach is clearly  $NZ$  times the time for a single propagation step. In case of angular spectrum propagation, a speedup by a factor of 2 can easily be obtained by starting with the object spectrum instead of the spatial object distribution. By precalculation of the propagator, which is constant for a fixed  $dz$ , only a multiplication and a back transformation needs to be carried out for each propagation step. The speed-up is 2, since the number of Fourier transforms is half of that of the brute force approach.

For a speed-up by more than a factor of 2, a different approach is needed.

If the x-y section is of size  $N \times N$ , we achieved an additional speedup by a factor of approx.  $2N$  by the following method.

The basic idea for this acceleration is the application of the Fourier projection theorem. It basically states that the on-axis value is the sum over all contributions of the input distribution. The theorem can be generalized for two dimensions and for an arbitrary  $x_0$  or  $y_0$  position by the following integral:

$$u_z(x, y_0) = \iint \tilde{u}_z(v, \mu) e^{2\pi i(vx + \mu y_0)} dv d\mu$$

$$= e^{2\pi i \mu y_0} \underbrace{\int \left( \int \tilde{u}_z(v, \mu) d\mu \right) e^{2\pi i v x} dv}_{\substack{\text{Projektion} \\ \text{1D-FFT}}} \quad (1)$$

The effort for one propagation step is therefore reduced from a two-dimensional Fourier transform to a one-dimensional projection and a one-dimensional Fourier transform.

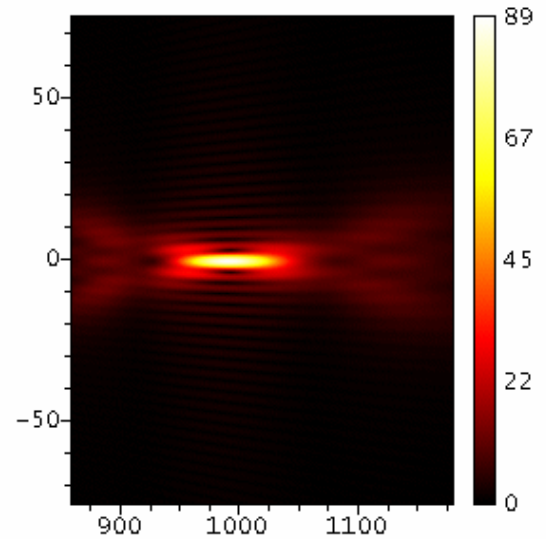


**Fig. 2:** x-z-Section of the focal amplitude for a thin lens with a parabolic phase profile and a numerical aperture of 0.15

Since the number of operations for a 2D-Fourier transform is  $2N^2ldN$  and number of operations for a 1D-Fourier transform is  $NldN$ , the additional speedup is

$$S = 2N \quad (2)$$

With this method, the time required for a 512x512 image can be reduced from a few minutes to a few seconds.

# On the true inclination factor under realistic focusing conditions

K.-H. Brenner

Light focusing is important in many applications of optics, like in particle trapping, laser welding or in optical storage. The standard treatment of a focusing lens was given by Richards and Wolf [1] as a vectorial extension of the scalar Debye approximation [2]. Although the work of Debye is mentioned in [1], a reference to this paper is missing there. The focal distribution in [1] is given as ( $\mathbf{s}_\perp = (s_x, s_y)$ )

$$\mathbf{e}(\mathbf{r}) = \frac{-ik}{2\pi} \iint_{\Omega} \frac{\mathbf{a}(\mathbf{s}_\perp)}{s_z} e^{ik(\Phi(\mathbf{s}_\perp) + \mathbf{s} \cdot \mathbf{r})} d^2 s_\perp \quad (1)$$

In Wolf's derivation, the conversion from a plane wave to a spherical converging wave was treated in an abstract way as a system, obeying the sine condition. The amplitude change follows from the law of energy conservation and results in the inclination factor

$$\mathbf{a}(\mathbf{s}_\perp) = f \cdot \sqrt{s_z} \cdot \mathbf{e}_1 \quad (2)$$

where the polarization vector  $\mathbf{e}_1$  follows from a decomposition of the incident field into TE- and TM-components which are transferred across the interface.

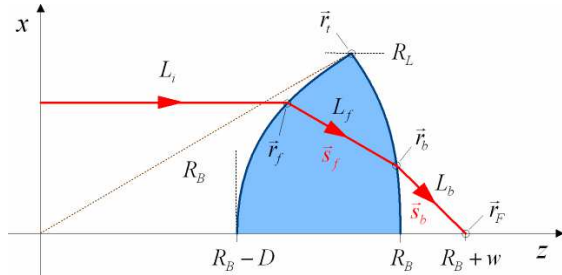


Fig. 1: Geometry of the perfect focussing lens

In this work, we have analyzed a realistic lens with perfect ray focusing properties (fig. 1). Since the polarisation treatment is the same as in [1], we only compared the pupil amplitude.

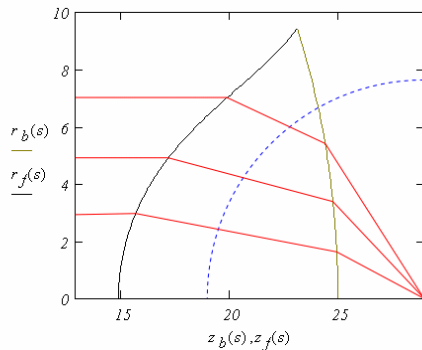


Fig. 2: Analytic shape of the front and back surface of a perfect focussing lens, together with three raypaths (red) and reference sphere for the paraxial  $f$  (blue).

We modeled the perfect focusing lens with aspheric front surface,  $n_{lens} = 1.52$  and spherical back surface

$R_B = 25\text{mm}$ , as shown in fig. 1. This problem can be solved analytically by using  $s$  as the  $x$ -component of  $\mathbf{s}_b$  as a parameter. Hence, both, the front surface  $\mathbf{r}_f(s)$  and the back surface  $\mathbf{r}_b(s)$  are available in an analytic form and can be plotted as shown in fig 2.

Using the law of energy conservation for the Poynting vectors

$$\mathbf{S}_{in}(s) d\mathbf{A}_{in} = \mathbf{S}_{out}(s) d\mathbf{A}_{out} \quad (3)$$

we can use the fact that the area element is planar at the input and spherical at the output. Thus the directions of  $\mathbf{S}$  and  $d\mathbf{A}$  agree in both cases. If we choose  $f$  as the paraxial focal length, we obtain

$$a(\mathbf{s}_\perp) = \frac{1}{f} \sqrt{\frac{s_z}{2s_\perp} \frac{\partial r_{f,\perp}^2(s_\perp)}{\partial s_\perp}} \quad (4)$$

which is to be compared with the inclination factor  $f \cdot \sqrt{s_z}$  from eq. 2. Figure 3 shows such a comparison with the Richards-Wolf result shown as blue, dotted curve and the inclination factor according to eq. 4 with  $NA=0.85$ ,  $R_L = 9.44\text{ mm}$  in red.

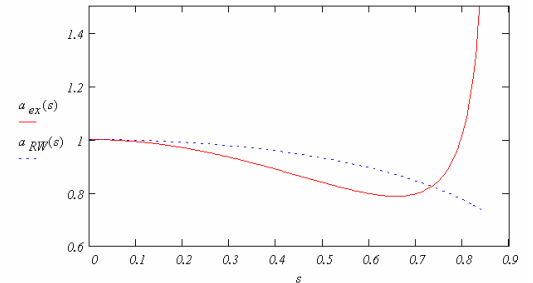


Fig. 3: True inclination factor (red) for a perfect focussing lens compared to the Richards-Wolf result (blue)

The pupil amplitude falls off more rapidly at small angles and increases strongly towards the lens edge, which results in sharper spots than predicted in [1]. These results are confirmed using the Fresnel formula.

## References:

- [1] B. Richards, E. Wolf, "Electromagnetic diffraction in optical systems, II. Structure of the image field in an aplanatic system," Proc. R. Soc. London Ser. A 253, 358–379 (1959).
- [2] P. Debye, "Das Verhalten von Lichtwellen in der Nähe eines Brennpunktes oder einer Brennlinie" Ann. Phys. 335(14), 755–776, (1909).

# Treatment of oblique illumination in numerical light propagation

*K.-H. Brenner*

In the thin-element-approximation (TEA), oblique illumination is usually treated by multiplying the input transmittance with the complex amplitude of a tilted plane wave, i.e.

$$u_0(x, y) = t(x, y) e^{i(k_x x + k_y y)} \quad (1)$$

For the object spectrum, this modulation results in a frequency shift, which increases the required real estate in the frequency domain - a problem, which has also been observed by Testorf [1].

The topic of this work is another, more serious problem with this method. In any numerical implementation, the true simulated object is a periodic replication of the central period. By multiplying the input transmittance with a tilted plane wave, the true operation is a multiplication with a sawtooth phase, since, unknowingly, we apply the same linear phase to each period. Fig. 1 illustrates this:

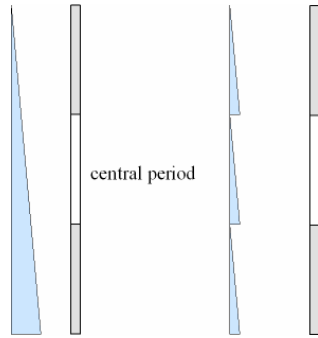


**Fig. 1:** Oblique illumination can be considered as a linear phase element. In a periodic situation, a sawtooth phase (right) is effectively applied instead of an infinitely extended linear phase (left).

If  $P$  is the calculation period, then only for certain angles,

$$\sin \vartheta = m \frac{\lambda}{P} \quad (2)$$

the phase step height is an integral multiple of  $2\pi$ . For all other angles, the neighbouring periods experience a constant phase shift, which differs in all periods. The effect of this error phase is hardly visible in most numerical calculations. The error, however, becomes very prominent in Talbot imaging. This can be explained very simple without any mathematics. At the Talbot distance, the Fresnel propagation phase is zero (or a multiple of  $2\pi$ ), which leads to a perfect amplitude and phase image of the input distribution. Assume, the input is a rectangular slit, the Talbot image will also be an unshifted rectangular slit with linear phase modulation. For a correct simulation, it

should, however, be a shifted slit. This simple example illustrates, that the error phase can lead to very severe errors.

Another example is a diffractive focusing element with long focal length  $f$ . If we record a line scan at  $z=f, y=0$  for different incident angles, we observe a light distribution shown in fig. 2.

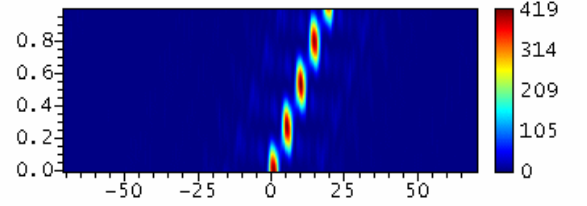


**Fig. 2:** Variation of focal intensity  $I(x,0,f)$  for incident angles from  $0^\circ$  to  $1^\circ$  using the standard method (eq. 1).

By rewriting the propagation equation, in such a way that the multiplication with the incident plane wave is replaced by a shift of the propagation phase,

$$\tilde{P}_z(\nu, \mu) = e^{ikz \sqrt{1 - (\lambda\nu + s_x)^2 - (\lambda\mu + s_y)^2}} \quad (3)$$

we obtain a very different simulation result (see fig. 3) for the same problem as in fig. 2. In eq. 3,  $s_x = \sin \vartheta \cos \varphi$ ,  $s_y = \sin \vartheta \sin \varphi$  are the lateral components of the unit direction vector of the incident plane wave.

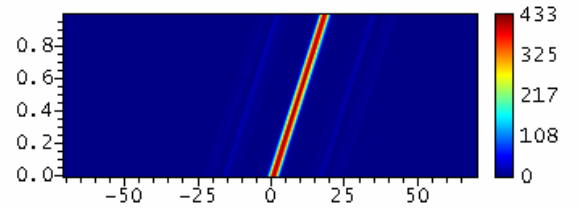


**Fig. 3:** Variation of focal intensity  $I(x,0,f)$  for incident angles from  $0^\circ$  to  $1^\circ$  using the modified method (eq. 3).

Now we obtain exactly, what is expected. The focal spot position shifts linearly with the incident angle. Thus the treatment of oblique illumination by eq. 3 not only avoids an increase in space-bandwidth product, but it also corrects the error phase terms.

## References:

- [1] M. E. Testorf, M. A. Fiddy: "Simulation of light propagation in planar-integrated free-space optics", *Opt. Commun.*, 176 (2000) 365-372.



# Imaging properties of a multi-spectral fluorescence microscope

*E. Slognat, P. Fischer, K.-H. Brenner*

The realized microscope setup is able to acquire images of four different fluorophores at the same point in time. The schematic setup is shown in Fig. 1.

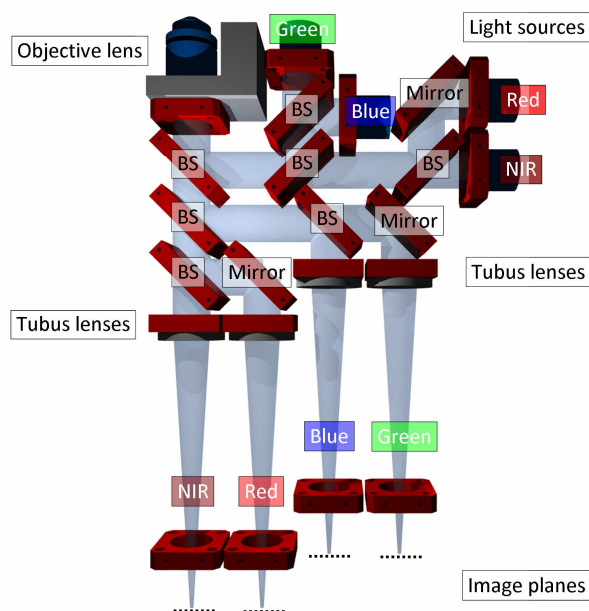


**Fig. 1:** Schematic setup of the multi-spectral fluorescence microscope

The resolution of each channel is analyzed by imaging a Siemens star with 30 spokes and a radius of  $400\ \mu\text{m}$  (Fig. 2). In order to be able to measure the magnification, it is surrounded by a square-shaped frame with a length of the edges of  $500\ \mu\text{m}$ . Due to the mainly spherical deformations of the used beam splitters, all channels show astigmatism except the NIR channel, where the beam splitters are only used in transmission.

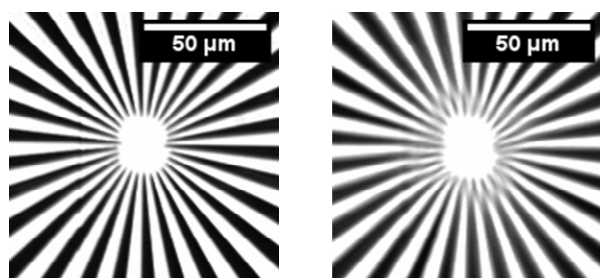


**Fig. 2:** Camera images of Siemens stars (left: NIR channel; right: red channel)

The resolution of the NIR channel is below  $1\ \mu\text{m}$ , of the red channel  $2.7\ \mu\text{m}$ , of the blue channel  $2.2\ \mu\text{m}$  and of the green channel  $2.5\ \mu\text{m}$ .

The NIR channel matches the ideal magnification of 10, whereas the other channels show slight deviations and produce smaller images of the object. This is

caused by the process of refocusing in order to compensate the astigmatism. The magnification in the red channel is 9.95, in the blue channel 9.82 and in the green channel 9.92.

High power LEDs are used as excitation light sources. Only in the red channel a halogen bulb - coupled into a fiber - is used, because there is no high power LED available which features the required spectrum. Fig. 3 shows the fluorescence images of the NIR and the red channel.

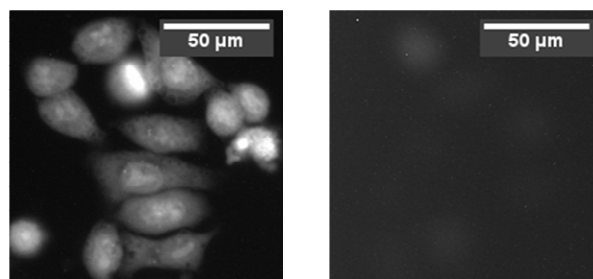


**Fig. 3:** Fluorescence images (left: NIR channel; right: red channel)

The exposure time of the NIR channel is 6 s, of the red channel 9.8 s, of the blue channel 80 ms and of the green channel 4 s.

It is striking that the exposure times of all channels except the blue channel are very high. Only in the blue channel an exposure time which makes fast scanning of the probe possible is achieved. The reason for these high exposure times is the low optical power of the light sources and the different quantum yields of the fluorophores. The blue channel features the light source with the highest optical power of 9.13 mW at the object plane, whereas the source in the red channel, where only an underexposed image at the maximum exposure time of the camera was obtained, has just an optical power of 0.85 mW.

## Conclusion

The blur of the images in the red, blue and green channels arises from the deformations of the beam splitters and can be eliminated by exchanging these elements through optical flat beam splitters. Then the obtained images will be as sharp as in the NIR channel.




Exposure times suitable for fast scanning microscopy can be achieved by using lasers instead of high power LEDs. Lasers which feature the required spectrum and optical power are available for each channel.

## PUBLICATIONS

1. INVITED: D. Wohlfeld, K.H. Brenner, "Aspects of short-range interconnect packaging", SPIE Photonics West Conference / Optoelectronic Interconnects XII, 8267-26, 24.-26.01.2012, San Francisco, USA, (2012)
2. M. Auer, K.-H. Brenner, "Calculation of Local Absorption in three-dimensional Structures using RCWA", 8th EOS Topical Meeting on Diffractive Optics, 27.02.-01.03.2012, ISBN 978-3-00-033711-6, Delft/NL, (2012)
3. K.-H. Brenner, "Optimization of local absorption in layered media", 8th EOS Topical Meeting on Diffractive Optics, 27.02.-01.03.2012, ISBN 978-3-00-033711-6, Delft/NL, (2012)
4. F. Merchà, K.-H. Brenner, „Novel integrated micro-optics system for the fabrication of Active Optical Cables“, Online-Zeitschrift der Deutschen Gesellschaft für angewandte Optik e. V., ISSN: 1614-8436-urn:nbn:de:0287-2012-B036-5, 113. Jahrestagung, 29. Mai-02. Juni 2012, Eindhoven, (2012)
5. E. Slognat, L. Lehmann, P. Fischer, K.-H. Brenner, "Concept and Implementation of a Compact Multi-Channel Fluorescence-Microscope Unit", Online-Zeitschrift der Deutschen Gesellschaft für angewandte Optik e. V., ISSN: 1614-8436-urn:nbn:de:0287-2012-P002-9, 113. Jahrestagung, 29. Mai-02. Juni 2012, Eindhoven, (2012)
6. K.-H. Brenner, R. Buschlinger, "Talbot Focusing – a new effect of periodic structures and its utilization", Online-Zeitschrift der Deutschen Gesellschaft für angewandte Optik e. V., ISSN: 1614-8436-urn:nbn:de:0287-2012-P040-7 113. Jahrestagung, 29. Mai-02. Juni 2012, Eindhoven, (2012)
7. INVITED: K.-H. Brenner, X. Liu, „High resolution wavefront sensing with non-interferometric techniques“, 11<sup>th</sup> Euro-American Workshop on Information Optics (WIO 2012), 20.-24. August 2012, Quebec, Kanada, (2012)
8. X. Liu, T. Stenau and K.-H. Brenner „Diffractive micro lens arrays with overlapping apertures“, 11<sup>th</sup> Euro-American Workshop on Information Optics (WIO 2012), 20.-24. August 2012, Quebec, Kanada, (2012)

# IMPRINT

**Publisher:** Prof. Dr. Karl-Heinz Brenner  
Chair of Optoelectronics  
Institute for Computer Engineering (ZITI)  
Ruprecht-Karls-University Heidelberg  
B6, 23-29, Bauteil C  
68131 Mannheim  
GERMANY

 +49 (0) 621 181 2700  
 +49 (0) 621 181 2695  
 <http://oe.ziti.uni-heidelberg.de>

**Layout:** K.-H. Brenner, M. Auer, X. Liu, S. Volk

**Type of publication:** Online

**Publication date:** 2013

## H I N W E I S

Alle Beiträge dieses Jahresberichts sind zitierbar.  
ISSN 2197 - 4462